Materials Advances

ROYAL SOCIETY OF CHEMISTRY

PAPER

View Article Online
View Journal | View Issue

Check for updates

Cite this: *Mater. Adv.*, 2020, **1**, 1849

A type-II blue phosphorus/$MoSe_2$ van der Waals heterostructure: improved electronic and optical properties *via* vertical electric field†

Huabing Shu

Building novel van der Waals (vdW) heterostructures is of great interest and is important to improve the performance of individual two-dimensional materials. Using first-principles calculations, we demonstrate that the constructed blue phosphorus/$MoSe_2$ (P_2/$MoSe_2$) vdW heterostructure has a unique type-II band alignment and a suitable bandgap (about 1.63 eV) for optoelectronic applications. Its electronic and optical properties depend strongly on the applied vertical electric field. The quasi-particle bandgap of the P_2/$MoSe_2$ can be linearly modulated by about 1.11 eV under the applied electric field and the type-II band alignment persists in a broad range. Meanwhile, the negative electric field induces a significant red-shift of the optical absorption edge of P_2/$MoSe_2$, greatly enhancing its absorption for the visible and near-infrared lights, which is desirable for optoelectronic applications. More importantly, the observed interlayer excitons with large binding energy (more than 600 meV) can be preserved under the applied electric field, being very much beneficial for the real separation of photoexcited carriers. These results indicate that the P_2/$MoSe_2$ vdW heterostructure can become a good candidate for optoelectronic devices.

Received 13th June 2020,
Accepted 23rd July 2020

DOI: 10.1039/d0ma00413h

rsc.li/materials-advances

Open Access Article. Published on 25 July 2020. Downloaded on 12/30/2025 10:04:13 AM.
This article is licensed under a Creative Commons Attribution-NonCommercial 3.0 Unported Licence.

1 Introduction

In recent years, the precise transfer of the produced two-dimensional (2D) materials has led to an emerging new class of materials, van der Waals (vdW) heterostructures.[1–8] vdW heterostructures, formed by vertically stacking two dissimilar 2D materials, can exhibit more desirable properties than their components due to interlayer coupling. For example, the interlayer coupling induced by vdW interactions can cause an ultrafast separation of photoexcited carriers[9–11] and long lifetimes of indirect excitons in the vdW heterostructure.[12,13] Such novel properties in vdW heterostructures can be utilized to explore their applications for photovoltaics and optoelectronics. Previously, an efficient flexible photovoltaic device based on graphene/MoS_2 was reported, achieving an external quantum efficiency of above 30%.[14] A p–n diode based on black phosphorene/MoS_2 obtains broad-band photodetection and sunlight harvesting.[15] The vdW heterostructures for other versatile applications also have been reported, including electrocatalysts,[16,17] Li^+/Na^+ ion batteries,[18,19] and supercapacitors.[20,21] In addition, the external electric field has also been considered as an effective way to further optimize the properties of vdW heterostructures. The electric-field tunable semiconductor-to-metal transition is observed in black phosphorene/MoS_2,[22] MoS_2/MX_2 (M: Mo, W, and Cr; X = Se, and S),[23] and black phosphorene (MoSSe)/blue phosphorene heterostructures,[24,25] suggesting a new application of these systems in semiconductor devices. More importantly, the external electric field can significantly manipulate the optical properties of the vdW heterostructure by changing the band alignment and interlayer coupling.[26,27] For example, in the WSe_2/graphene vdW heterostructure, the external electric field enhances photoluminescence (PL) intensity of excitons by more than 40 times and induces a maximum blue-shift of 50 meV of exciton peaks.[28]

Among 2D materials, the hexagonal $MoSe_2$ monolayer has desirable properties, such as a direct bandgap of 1.60 eV,[29,30] optical absorbance of 5–10% for the incident sunlight, and a photo flux of 4.6 mA cm^{-2}.[31] Monolayer $MoSe_2$-based field effect transistors can also obtain an on/off current ratio as high as 10^6 and an intrinsic carrier mobility of up to 500 cm^2 V^{-1} s^{-1} at 100 K.[32] In 2016 the blue phosphorus (P_2) monolayer with in-plane hexagonal structure was firstly synthesized on Au(111) by a molecular beam epitaxial growth approach.[33] Furthermore, theoretical studies have demonstrated that it has intriguing structural and electronic properties, such as its stability at room temperature,[34,35] moderate bandgap of approximately 2.0 eV,[35,36] and room-temperature carrier mobility of over

School of Science, Jiangsu University of Science and Technology, Zhenjiang 212001, China. E-mail: shuhuabing@just.edu.cn

† Electronic supplementary information (ESI) available. See DOI: 10.1039/d0ma00413h

Open Access Article. Published on 25 July 2020. Downloaded on 12/30/2025 10:04:13 AM.
This article is licensed under a Creative Commons Attribution-NonCommercial 3.0 Unported Licence.

10^3 cm^2 V^{-1} s^{-1}.[37] These good properties in $MoSe_2$ and P_2 monolayers can draw enormous interest, suggesting great potential in optoelectronic devices. Besides, the $MoSe_2$ and P_2 monolayers with similar hexagonal structure[35,38] have distinct differences in constituents and chemical bonding, which may form a large potential difference and band offsets between the two layers. Meanwhile, it suggests that the hybrid band structure, band alignment at the heterointerface, and even interlayer coupling in the vdW heterostructure based on $MoSe_2$ and P_2 monolayers, can be manipulated by an external electric field. Previously, $MoSe_2$-based vdW heterostructures, such as WS_2/$MoSe_2$[39,40] and WSe_2/$MoSe_2$,[41] have been achieved by transfer methods. Therefore, the fabrication of a P_2/$MoSe_2$ vdW heterostructure is anticipated and their properties are of great interest.

In this work, we construct five P_2/$MoSe_2$ vdW heterostructures by stacking the P_2 and $MoSe_2$ monolayers. Using density-functional theory (DFT) connected with the G_0W_0 + Bethe–Salpeter equation (BSE) method, we investigated the P_2/$MoSe_2$ vdW heterostructure, focusing on the structure, electronic and optical properties, and the effect of vertical electric field. Our calculations show that its electronic band structure and optical response are very sensitive to the size and orientation of the applied electric field.

2 Computational method

The electronic and optical properties of the systems were attained *via* a three-step procedure. First, we used a plane-wave basis set and a norm-conserving pseudopotential[42] to achieve the ground states, which was performed by the Quantum Espresso code.[43] Electron exchange and correlation were treated by generalized gradient approximation (GGA) along with the Perder–Burke–Ernzerhof (PBE) functional.[44] The $4s^24p^64d^55s^1$ of Mo, $4s^24p^6$ of Se, and $3s^23p^3$ of P were used as valence electrons. The cutoff energy for wave function was set to be 70 Ry. To eliminate the interaction between spurious replicate images, a vacuum region of 20 Å along the *c*-axial direction was inserted for the systems. The Brillouin zone integrations adopted a *k*-point grid of $18 \times 18 \times 1$. The weak interaction between two layers was considered *via* a vdW-DF approach.[45,46] When structures were fully relaxed, the force applied on each atom and the total energy of the system were converged within the 0.01 eV $Å^{-1}$ and 10^{-4} eV, respectively. To avoid the errors induced by the periodic boundary condition, dipole correction was considered in the systems. Furthermore, an external sawtooth potential along the *c*-axial direction was also used to simulate the effect of an applied electric field.[47] The phonon dispersion relations of the systems were obtained by performing phonon calculations from density functional perturbation theory.[48]

Then, the G_0W_0 approximation[49] was used to obtain quasi-particle (QP) band structures. The convergence of quasi-particle bandgap with respect to the number of unoccupied bands, the size of dielectric matrix and the *k*-point grid was carefully checked and a convergence of 100 meV was assured in the systems. Finally, the coupled electron–hole excitation energies and exciton wave functions were obtained by solving the Bethe–Salpeter equation (BSE).[50,51] The 1218 bands (unoccupied bands: 1200, and occupied bands: 18) and random phase approximation were involved to attain the converged dielectric function. A fine *k*-point grid ($54 \times 54 \times 1$), 38 bands (20 unoccupied bands), was utilized to obtain the converged optical spectra. The G_0W_0 and BSE calculations were performed *via* the YAMBO code.[52]

3 Results and discussion

3.1 Geometric structure and stability

Before investigating the P_2/$MoSe_2$ vdW heterostructure, it is necessary to understand the geometries and electronic properties of P_2 and $MoSe_2$ monolayers. Their optimized geometric structures are provided in Fig. S1 of the ESI,† in which the lattice constants are $a_{P_2} = b_{P_2} = 3.322$ Å for the P_2 monolayer and $a_{MoSe_2} = b_{MoSe_2} = 3.269$ Å for the $MoSe_2$ monolayer. The bond lengths of P–P and Mo–Se are 2.271 Å and 2.549 Å, respectively. The obtained structural parameters are in good accordance with previous studies.[35,53,54] To examine the electronic properties of the P_2 and $MoSe_2$ monolayers, the quasi-particle band structures with many-body interaction included, are calculated by the single-shot G_0W_0 method and the results are exhibited in Fig. S2 (ESI†). It can be found that the P_2 monolayer is an indirect semiconductor with a wide quasi-particle gap of 3.350 eV, while the $MoSe_2$ monolayer has a direct bandgap of 2.300 eV at *K*-point. Interestingly, the gap of the $MoSe_2$ monolayer is fixed at the visible-light region, suggesting its potential for visible-light-driven optoelectronics. The predicted quasi-particle bandgaps agree well with previous reports (3.530 eV for P_2 monolayer; 2.260 eV for $MoSe_2$ monolayer).[54–56]

Due to small lattice mismatch (approximately 1.6%) between the P_2 and $MoSe_2$ monolayers, five P_2/$MoSe_2$ vdW heterostructures are constructed by the 1×1 primitive cells of the P_2 and $MoSe_2$ monolayers, as shown in Fig. 1. The lattice mismatch is calculated by $2(a_{P_2} - a_{MoSe_2})/(a_{P_2} + a_{MoSe_2})$. To verify the thermal stability of the five possible stacking configurations, the formation energies (E_f) are firstly calculated to assess them using the equation $E_f = E_1 - E_2 - E_3$, where E_1, E_2, and E_3 are the total energies of the P_2/$MoSe_2$, P_2 monolayer, and $MoSe_2$ monolayer, respectively. The estimated formation energies are all negative for these designed configurations (as seen in Table S1, ESI†), suggesting that the fabrications of P_2/$MoSe_2$ vdW heterostructures should be feasible from a thermodynamic point of view. Among these constructed vdW heterostructures, the AA-I stacking shows the most stable structure by the lowest formation energy of −0.212 eV per unit cell. We further verify the dynamical stability of these heterostructures by calculating their phonon spectra, which are shown in Fig. 2(b)–(f). The observed phonon spectra of AA-I and AB-III stacking structures have no negative frequencies, while the other three stacking configurations (AA-II, AB-I, and AB-II) have negligible imaginary frequencies around the Γ-point. The calculation results of phonon dispersion indicate that the AA-I and AB-III configurations have more dynamical stability than the other three configurations.

 This journal is © The Royal Society of Chemistry 2020

Open Access Article. Published on 25 July 2020. Downloaded on 12/30/2025 10:04:13 AM.
This article is licensed under a Creative Commons Attribution-NonCommercial 3.0 Unported Licence.

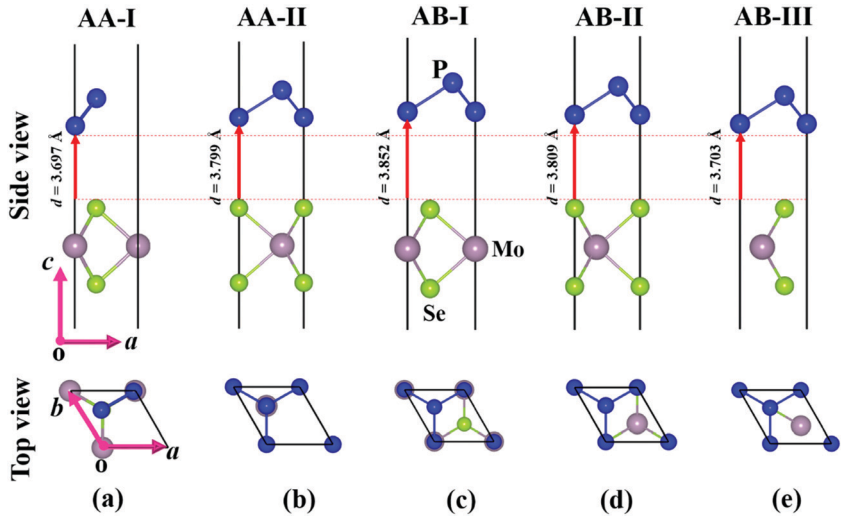

Fig. 1 Optimized structures of $P_2/MoSe_2$ vdW heterostructures with different stacking configurations: (a) AA-I, (b) AA-II, (c) AB-I, (d) AB-II, and (e) AB-III.

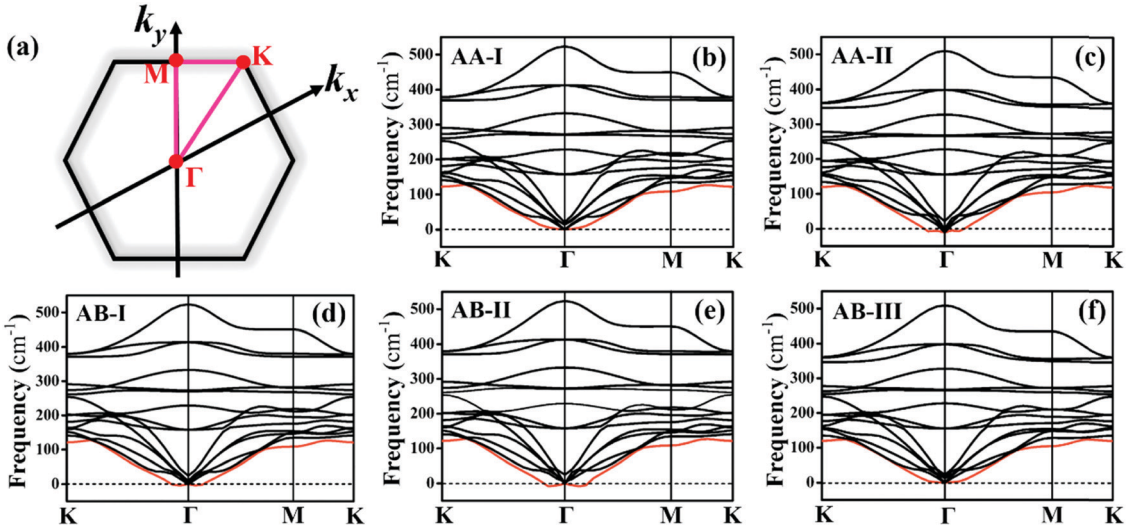

Fig. 2 (a) High-symmetric path (K–Γ–M–K) of the first Brillouin zone of hexagonal lattice, K (1/3, 1/3, 0), Γ (0, 0, 0), and M (0, 1/2, 0). Phonon spectra of $P_2/MoSe_2$ vdW heterostructures with different stacking configurations: (b) AA-I, (c) AA-II, (d) AB-I, (e) AB-II, and (f) AB-III.

In addition, as a comparison, the structural parameters of the five configurations are also listed in Table S1 (ESI†). There is little difference in the lattice constant, bond length, and interlayer distance for the five stacking configurations, which will result in similar band dispersion, as seen in Fig. S3 (ESI†). In the following sections, we only investigate the most stable AA-I configuration among five stacking configurations.

3.2 Electronic and optical properties

Fig. 3(a) shows the quasi-particle band structure of the AA-I stacking $P_2/MoSe_2$ vdW heterostructure at the single-shot G_0W_0 level. Compared with the isolated P_2 and $MoSe_2$ monolayers, the $P_2/MoSe_2$ vdW heterostructure has a relatively narrow indirect gap of 1.630 eV due to the preserved band structures of the two monolayers. This phenomenon has also been observed in other semiconducting vdW heterostructures, such as WS_2/MoS_2, blue phosphorene/BSe, and blue phosphorus/$Mg(OH)_2$.[58–60] To understand the layer contributions to the highest occupied state (VBM) and the lowest unoccupied state (CBM) of the $P_2/MoSe_2$, the partial charge distributions of the CBM and VBM are calculated and the results are exhibited in Fig. 3(a) right. It is found the CBM and VBM of the $P_2/MoSe_2$ are contributed by the P_2 and $MoSe_2$ layers, respectively, suggesting it has a type-II characteristic of band alignment and good charge separation. To check the charge transfer between the P_2 and $MoSe_2$ layers, it is necessary to obtain the work functions (Φ) of the isolated P_2 and $MoSe_2$ monolayers. The Φ can be calculated by the definition: $\Phi = E_{VAC} - E_{VBM}$, in which E_{VAC} and E_{VBM} are the vacuum potential and VBM energy, respectively.[61] The obtained work functions are 6.96 eV for the P_2 monolayer and 5.46 eV for the $MoSe_2$ monolayer, respectively. Owing to a relatively large difference (1.50 eV) in the work functions

Open Access Article. Published on 25 July 2020. Downloaded on 12/30/2025 10:04:13 AM.
This article is licensed under a Creative Commons Attribution-NonCommercial 3.0 Unported Licence.

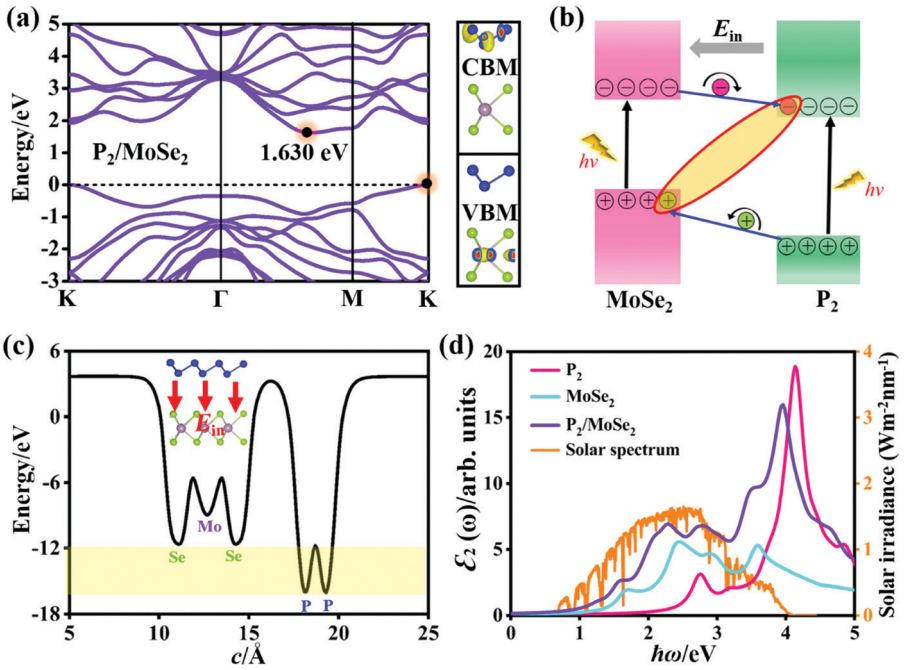

Fig. 3 (a) Quasi-particle band structure and decomposed charge density (CBM and VBM) of the $P_2/MoSe_2$ vdW heterostructure (isosurface: 3.0×10^{-3} e Å^{-3}). (b) Schematic diagram of the band alignment between the two layers in $P_2/MoSe_2$ and charge separation at the P_2–$MoSe_2$ interface. (c) Planar average electrostatic potential of the $P_2/MoSe_2$ along the *c*-axial direction. The direction of built-in electric field (E_{in}) is inset. (d) Optical absorption spectra of the P_2 and $MoSe_2$ monolayers, and $P_2/MoSe_2$ including the interaction between photoexcited electrons and holes, in comparison with the incident AM 1.5G solar irradiance.[57] Polarized light along the *a*-axial direction and Lorentzian broadening (0.15 eV) are used in these spectra.

between the P_2 and $MoSe_2$ monolayers, electrons can easily migrate from the $MoSe_2$ layer into the P_2 layer after forming the $P_2/MoSe_2$ vdW heterostructure. The work function of $P_2/MoSe_2$ is also estimated to be 4.95 eV, being less than those of the isolated monolayers due to the interlayer coupling. Also, the calculated two band edges of the heterostructure relative to the vacuum level are located at −3.32 eV (CBM) and −4.95 eV (VBM), which cannot wholly straddle water redox potentials (reduction potential: −4.44 eV; oxidation potential: −5.67 eV) at pH = 0. However, the $P_2/MoSe_2$ vdW heterostructure satisfies the reduction level in water splitting. Upon illuminating the $P_2/MoSe_2$, the photoexcited electrons collected in the P_2 layer due to the type-II band alignment will drive the hydrogen reduction reaction generating hydrogen ($2H^+ + 2e^- \rightarrow H_2$), as shown in Fig. S4 (ESI†), suggesting it could be a potential hydrogen production material.

Fig. 3(b) shows the charge separation at the P_2–$MoSe_2$ interface and the formation of indirect excitons when illuminating the $P_2/MoSe_2$ vdW heterostructure. The photoexcited electrons and holes are inclined to spontaneously separate into the opposite layers by the potential offsets. The formed indirect excitons will prolong the lifetime of photoexcited carriers, being very useful for optoelectronic devices. In fact, the indirect charge-transfer exciton has been observed experimentally in other vdW heterostructures (like MoS_2/WS_2, $MoS_2/MoSe_2$, and MoS_2/WSe_2) by time resolved measurements[9,62] and photoluminescence quenching.[58,63,64] In addition, the planar average electrostatic potential is also computed and presented in Fig. 3(c). The depth of potential of the $MoSe_2$ layer is smaller than that of the P_2 layer by about 4 eV, indicating that the built-in electric field (E_{in}) has been formed in the $MoSe_2$–P_2 interface. The direction of the E_{in} is pointed from the P_2 layer to the $MoSe_2$ layer (as seen in the inset of Fig. 3(c)), which will play an important role in further facilitating charge separation, *i.e.* the photoexcited electron (hole) is accelerated to flow from the $MoSe_2$ (P_2) layer to the P_2 ($MoSe_2$) layer under the E_{in} (as in Fig. 3(b)). As a result, the E_{in} can promote the separation of photoexcited electron–hole pairs in the $P_2/MoSe_2$ vdW heterostructure.

On the other hand, the excitonic behavior of the $P_2/MoSe_2$ vdW heterostructure should have a striking difference with those of the isolated P_2 and $MoSe_2$ monolayers owing to the existence of a potential gradient across the P_2–$MoSe_2$ interface. In order to obtain their exact optical properties, we solved the BSE equation based on the G_0W_0 calculations, which has fully included the many-body interactions (electron–electron and electron–hole interactions) in real systems. Fig. 3(d) shows the imaginary parts $\varepsilon_2(\omega)$ of the dielectric functions of the P_2 monolayer, $MoSe_2$ monolayer, and the $P_2/MoSe_2$ heterostructure, *i.e.* the optical absorption spectra. It can be found that the $P_2/MoSe_2$ heterostructure has a wide absorption range from the near-infrared to the near-ultraviolet. The optical spectrum of the $P_2/MoSe_2$ is dominated by the $MoSe_2$ layer in the energy of 0–2 eV, while the absorption ranging from 2 eV to 5 eV is contributed by both the $MoSe_2$ and P_2 layers. Compared with the isolated P_2 and $MoSe_2$ monolayers, the $P_2/MoSe_2$ vdW heterostructure has a marked enhancement of optical absorption in a broad light-harvesting range, spanning from 1.64 eV

 This journal is © The Royal Society of Chemistry 2020

Open Access Article. Published on 25 July 2020. Downloaded on 12/30/2025 10:04:13 AM.
This article is licensed under a Creative Commons Attribution-NonCommercial 3.0 Unported Licence.

(visible light) to 4.15 eV (near-ultraviolet light). The enhanced optical absorption in the $P_2/MoSe_2$ vdW heterostructure should originate from the interlayer coupling and charge transfer between the two single layers as well as the overlap of the electronic states. In addition, for the incident AM 1.5G solar irradiance, the $P_2/MoSe_2$ vdW heterostructure can also absorb a considerable part, as shown in Fig. 3(d), which could be used in optoelectronic devices based on the solar irradiance.

3.3 Effects of vertical electric fields on electronic and optical properties

To explore the effect of electric field on the electronic properties of the $P_2/MoSe_2$ vdW heterostructure, an electric field (E_{ef}) perpendicular to the stacking layers is applied on the heterostructure, ranging from -0.4 V Å^{-1} to 0.4 V Å^{-1} with the step of 0.1 V Å^{-1}. The phonon spectrum of $P_2/MoSe_2$ at the electric field of 0.4 V Å^{-1} is also calculated to check its dynamical stability, as presented in Fig. S5 (ESI†). Only a small imaginary frequency of -1.8 cm^{-1} close to the Γ point is observed in the $P_2/MoSe_2$, suggesting it has dynamic stability under the observed electric field. The positive direction of vertical electric field is pointed from the $MoSe_2$ layer to the P_2 layer along the *c*-axial direction. Experimentally, a controlled vertical electric field can be realized by a double-gated configuration without changing the charge carrier concentration in the $P_2/MoSe_2$ vdW heterostructure, as shown in Fig. 4(a). Fig. 4(b) shows the various bandgaps under different electric-field strengths from the PBE and G_0W_0 methods. The G_0W_0 method can correct the band structure of the semiconductor at the PBE level to obtain a credible quasi-particle bandgap by shifting the conduction (valence) band up (down). It can be seen that the quasi-particle bandgap of the $P_2/MoSe_2$ heterostructure can be significantly tuned in a wide range from 0.94 eV ($E_{ef} = -0.4$ V Å^{-1}) to 2.05 eV (E_{ef} = 0.4 V Å^{-1}). Although the PBE method underestimates the bandgap of the semiconducting material, the trend of bandgap variation in the two methods is roughly the same in the observed electric field range, in which the bandgap linearly increases with E_{ef} from -0.4 V Å^{-1} to 0.24 V Å^{-1} and shows little change from 0.24 V Å^{-1} to 0.4 V Å^{-1}. To shed more light on the variable bandgap, the projected band structures of $P_2/MoSe_2$ under variable electric fields is calculated and presented in Fig. 5(a)–(e). It is found that the CBM (A point) belonging to the P_2 layer is very sensitive to E_{ef}, in which the A point is slowly elevated in the range of -0.4 to 0.2 V Å^{-1}, leading to the increasing bandgap of the $P_2/MoSe_2$. In fact, the CBM has been shifted to the B point located at the $MoSe_2$ layer at E_{ef} = 0.24 V Å^{-1}, shown in Fig. 5(f), suggesting that the type-II band alignment in the $P_2/MoSe_2$ heterostructure is converted to type-I at E_{ef} = 0.24 V Å^{-1}. When the E_{ef} is larger than 0.24 V Å^{-1}, the invariable bandgap of the $P_2/MoSe_2$ should be attributed to the insensitive B point to the applied electric field. Interestingly, for the $P_2/MoSe_2$ vdW heterostructure, the retained type-II heterointerface in a wide range from -0.4 to 0.24 V Å^{-1}, together with broadly tunable bandgap, will endow it with potential applications in the optoeletronics and solar energy conversion.

To obtain more physical insight into the $P_2/MoSe_2$ heterostructure, the planar-averaged electron density difference is also calculated along the *c*-axial direction under the E_{ef}, as shown in Fig. 6. When applying an enhanced positive E_{ef}, more electrons (Δq) flow from the P_2 layer to the $MoSe_2$ layer, which will generate an interlayer dipole moment *P*, causing the electric polarized field E_{epf} across the interlayer region of the $P_2/MoSe_2$. The direction of the E_{epf} points from the P_2 layer to the $MoSe_2$ layer, being opposite with the positive direction of the E_{ef}. Such an E_{epf} across the P_2–$MoSe_2$ interface is beneficial to the separation of photoexcited carriers on the interface, shown in Fig. S6 (ESI†). On the contrary, more electrons tend to transfer from the $MoSe_2$ layer to the P_2 layer under an increased reverse E_{ef}. Bader charge analysis further verifies that $\Delta q = 1.15 \times 10^{-2}$ *e*, 4.9×10^{-3} *e*, and -1.2×10^{-3} *e* are transferred from the P_2 layer to $MoSe_2$ layer at E_{ef} = 0.4 V Å^{-1}, 0 V Å^{-1}, and -0.4 V Å^{-1}, respectively. Furthermore, the magnitude of electric polarized field (E_{epf}) can be estimated by $E_{epf} = P/\varepsilon_0 \cdot \varepsilon_r \cdot S_0 \cdot d$. *P* is the size of the dipole moment and $P = |\Delta q| \cdot d$, ε_0 and ε_r are the permittivity of free space and relative dielectric constant ($\varepsilon_0 = 8.850 \times 10^{-12}$ F m^{-1}, $\varepsilon_r = 1.0$), respectively, S_0 is the interface area of the $P_2/MoSe_2$ ($S_0 = 9.380 \times 10^{-20}$ m^2), and *d* is the interlayer equivalent distance ($d = 3.697 \times 10^{-10}$ m). The calculated E_{epf} under different E_{ef} values can be found in Table S2 (ESI†). When E_{ef} is strengthened to 0.40 V Å^{-1}, the induced E_{epf} with opposite direction can be as large as 0.22 V Å^{-1}, which is comparable to the applied vertical electric field. Thus, the vertical electric field

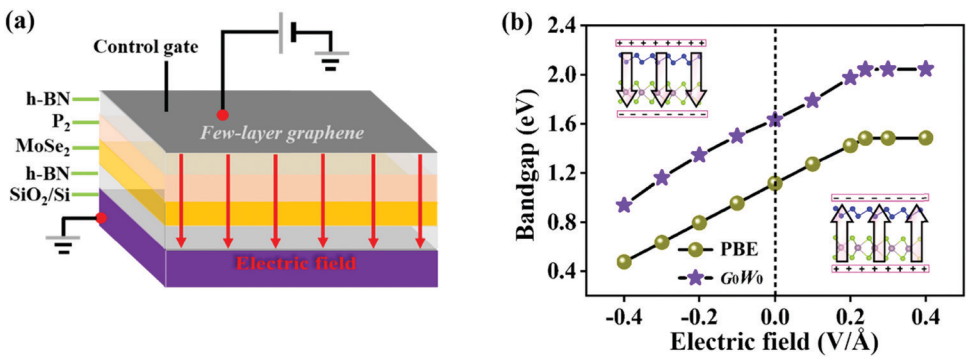

Fig. 4 (a) Schematic of double-gated $P_2/MoSe_2$ device. (b)Evolution of bandgap as a function of the vertical electric field in the $P_2/MoSe_2$ vdW heterostructure. Two insets show the positive and negative directions of the vertical electric field, respectively.

Open Access Article. Published on 25 July 2020. Downloaded on 12/30/2025 10:04:13 AM.
This article is licensed under a Creative Commons Attribution-NonCommercial 3.0 Unported Licence.

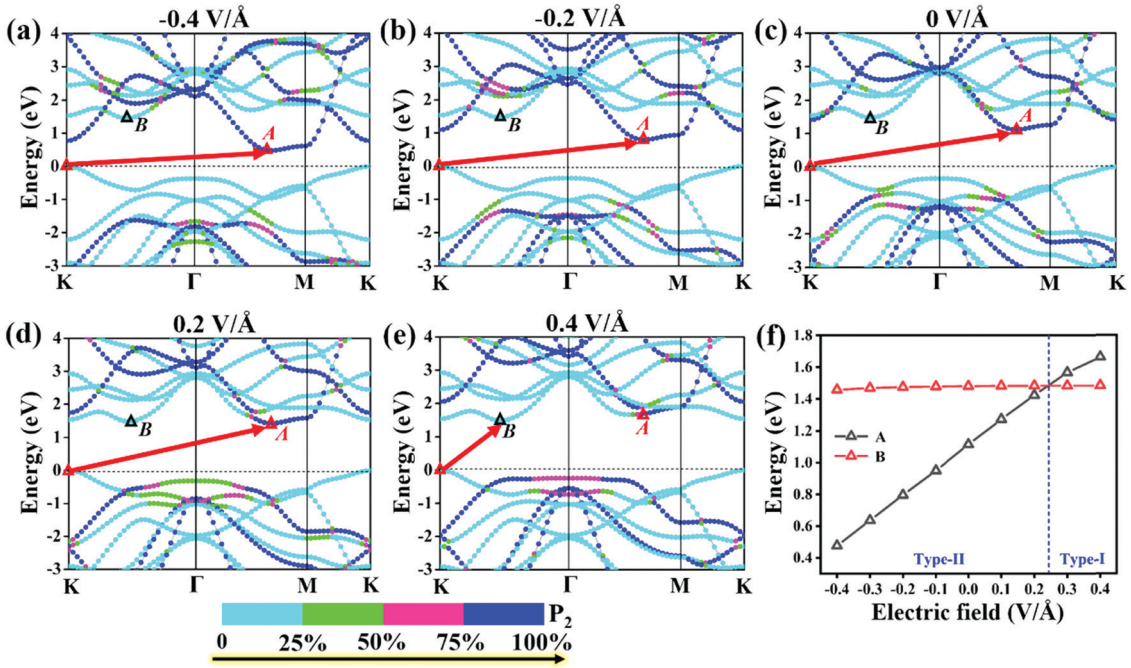

Fig. 5 (a)–(e) Projected band structures of the $P_2/MoSe_2$ vdW heterostructure and (f) relative positions of "A" and "B" to the VBM at PBE level under a variable electric field.

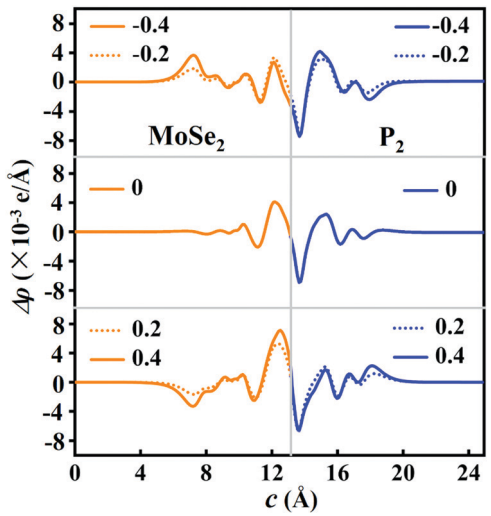

Fig. 6 Planar-averaged electron density difference across the $P_2/MoSe_2$ vdW heterostructure under various electric fields of −0.4 V Å^{-1}, −0.2 V Å^{-1}, 0 V Å^{-1}, 0.2 V Å^{-1}, and 0.4 V Å^{-1}. The orange (blue) region corresponds the the $MoSe_2$ (P_2) layer.

may not only effectively tailor the carrier concentrations of the $MoSe_2$ and P_2 layers, but also change the interlayer coupling at the P_2–$MoSe_2$ heterointerface.

As mentioned before, there is a significant difference in the band structure of the $P_2/MoSe_2$ vdW heterostructure under different vertical electric fields. To further investigate the variation in the optical properties of the $P_2/MoSe_2$ at different electric field strengths, we calculated the $\varepsilon_2(\omega)$ of the $P_2/MoSe_2$ at electric fields of −0.4 V Å^{-1}, 0 V Å^{-1}, and 0.4 V Å^{-1} and the results are plotted in Fig. 7, in which two polarized lights along the zigzag (*a*-axial) and armchair directions are adopted, respectively. From Fig. 7(a)–(c), strong isotropy is observed between ε_2 (zigzag) and ε_2 (armchair), suggesting that the isotropic nature of optical absorption in the $P_2/MoSe_2$ vdW heterostructure can be retained under the observed electric fields. When the negative electric field is applied on the $P_2/MoSe_2$, its absorption edge moves toward low energy (as seen in Fig. 7(d)), enhancing the optical absorption for the near-infrared and visible lights. The red-shift of the optical spectrum originates from the decrease of the bandgap of the $P_2/MoSe_2$ under the negative electric field, while the positive electric field pushes the absorption edge to a high-energy region due to the increase of bandgap. The blue-shift of the absorption edge results in the blue-shift of the highest absorption peak, positioned at 3.535 eV, 3.944 eV, and 4.135 eV for −0.4 V Å^{-1}, 0 V Å^{-1}, and 0.4 V Å^{-1}, respectively. Meanwhile, the intensity of the highest peak is strengthened from −0.4 V Å^{-1} to 0.4 V Å^{-1}, suggesting that the absorption of the $P_2/MoSe_2$ for the near-ultraviolet light becomes more active under the positive electric field.

Fig. 8 shows the calculated oscillator strengths of the excited states of the $P_2/MoSe_2$ vdW herterostructure under the electric field of −0.4 V Å^{-1}, 0 V Å^{-1}, and 0.4 V Å^{-1}, suggesting that the vertical electric field can significantly influence the photo-excited behavior of $P_2/MoSe_2$. Based on the oscillator strength selection rules, we analyze the transition of $P_2/MoSe_2$ under the three electric fields. For the primitive $P_2/MoSe_2$ vdW heterostructure, the low-energy spectrum of 0–2 eV is mainly contributed by the $MoSe_2$ layer (as seen in Fig. 3(d)), which means that the intralayer excitons of the $MoSe_2$ layer dominate the

 This journal is © The Royal Society of Chemistry 2020

Open Access Article. Published on 25 July 2020. Downloaded on 12/30/2025 10:04:13 AM.
This article is licensed under a Creative Commons Attribution-NonCommercial 3.0 Unported Licence.

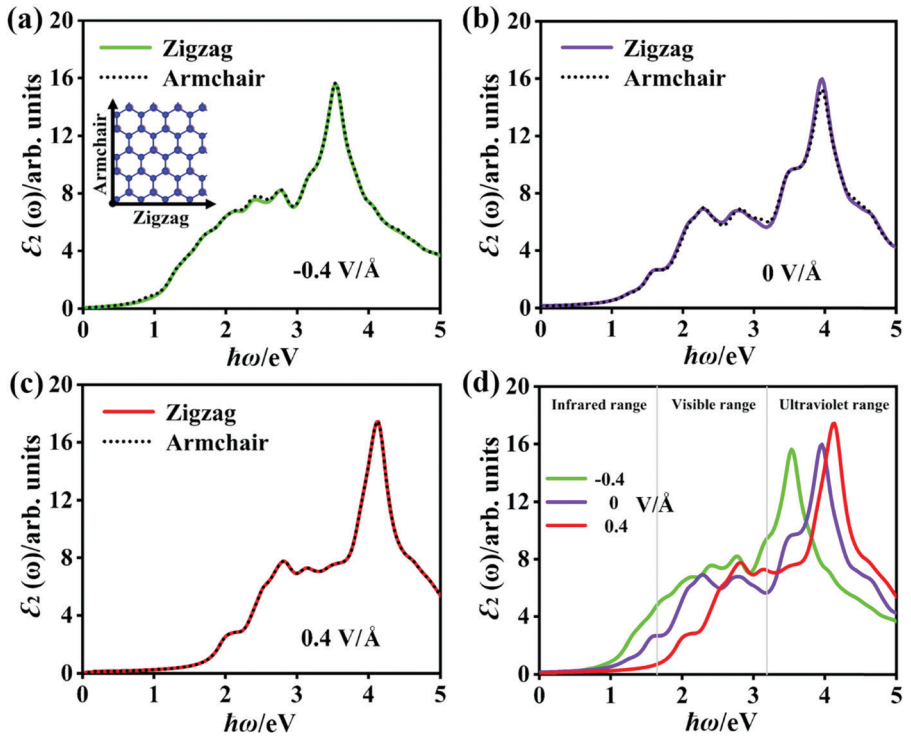

Fig. 7 (a)–(c) The optical absorption spectra of the $P_2/MoSe_2$ vdW herterostructure along the two polarized-light directions (Zigzag and Armchair) at the vertical electric fields of −0.4 V Å^{-1}, 0 V Å^{-1}, and 0.4 V Å^{-1}. The Zigzag and Armchair directions are inset. These calculated spectra have included the electron–hole interaction. (d) The comparable optical absorption spectra along the zigzag polarized-light direction (*i.e.* the *a*-axial direction) under different electric fields. A Lorentzian broadening of 0.15 eV is applied in the calculations of the optical spectra.

low-energy spectrum. However, an active interlayer transition is also found at the energy position of about 1.26 eV, which comes from the vertical transition between the VBM and CBM at certain non-high-symmetric point *T*(5/18, 1/3, 0) near high-symmetric *K* point. The partial charge distributions of VBM and CBM at the *T* point can be found in Fig. S7 (ESI†), in which the VBM (CBM) is mainly contributed by the $MoSe_2$ (P_2) layer. Another inactive interlayer transition is also observed at about 1.05 eV although its oscillator strength is very small (as seen in the inset of Fig. 8(b)), which is mainly between the VBM and CBM at the *K* point. The active interlayer transition can induce the formation of an interlayer exciton (*i.e.* indirect exciton), whose binding energy is estimated to be 670 meV by the method of the energy difference between the quasi-particle energy and excitation energy. For the cases of −0.4 V Å^{-1} and 0.4 V Å^{-1}, active interlayer transitions occur at 1.50 eV and 1.82 eV, respectively (marked in Fig. 8(a) and (c)), which generate two corresponding interlayer excitons. For the −0.4 V Å^{-1}, the active interlayer transition comes from the vertical transition between the VBM ($MoSe_2$ layer) and CBM (P_2 layer) at the *K* point, which is different to that of the primitive $P_2/MoSe_2$, while the active interlayer transition under the electric field of 0.4 V Å^{-1} is from the VBM ($MoSe_2$ layer) to the second conduction band (P_2 layer) at the *K* point. The two observed interlayer excitons also possess considerable binding energies of 614 meV for −0.4 V Å^{-1} and 628 meV for 0.4 V Å^{-1}, which is comparable with that of the primitive $P_2/MoSe_2$.

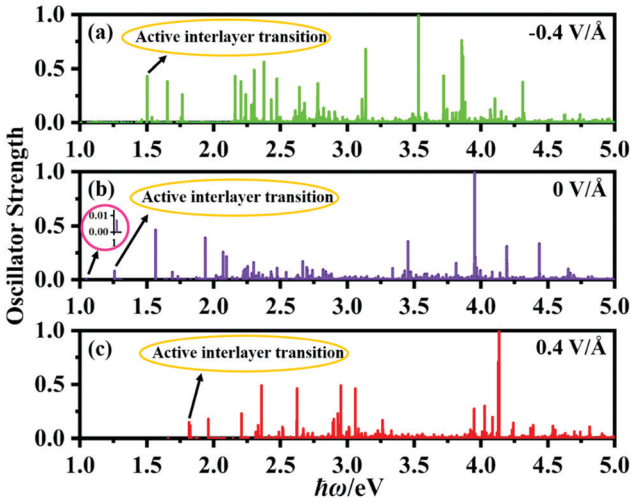

Fig. 8 (a)–(c) Calculated oscillator strengths of excited states of the $P_2/MoSe_2$ vdW herterostructure in the energy range of 1–5 eV for vertical electric fields of −0.4 V Å^{-1}, 0 V Å^{-1}, and 0.4 V Å^{-1}. The polarized light is along the zigzag direction.

These interlayer excitons found in the $P_2/MoSe_2$ heterostructure are beneficial to facilitate the separation of photoexcited carriers, which is very important for applications in photovoltaics and photocatalytic water splitting. On the basis of the above results, we can draw a conclusion that the bandgap of the $P_2/MoSe_2$ vdW heterostructure can be modulated in a broad range and its

Open Access Article. Published on 25 July 2020. Downloaded on 12/30/2025 10:04:13 AM.
This article is licensed under a Creative Commons Attribution-NonCommercial 3.0 Unported Licence.

optical properties can also be tuned effectively by applying the vertical electric field.

4 Conclusions

In summary, we performed first-principles calculations to investigate the effect of vertical electric field on the electronic and optical properties of the constructed $P_2/MoSe_2$ vdW heterostructure. We found that the AA-stacking $P_2/MoSe_2$ with more stability has an intrinsic type-II band alignment, in which photoexcited electrons (holes) migrate from the $MoSe_2$ (P_2) to the P_2 ($MoSe_2$) layer. The estimated quasi-particle bandgap can be tuned effectively from 0.94 eV (-0.4 V Å^{-1}) to 2.05 eV (0.4 V Å^{-1}) by the vertical electric field. A transition from type-II to type-I can be observed under a moderate electric field of 0.24 V Å^{-1}. More interestingly, $P_2/MoSe_2$ possesses a strong and broad optical absorption ranging from the near-infrared to near-ultraviolet. Under the negative electric field, the optical absorption of the $P_2/MoSe_2$ heterostructure for the visible and near-infrared light can be enhanced significantly. The active interlayer excitons with binding energy more than 600 meV are observed under the applied vertical electric field, being favorable to effectively separate the photoexcited electron–hole pairs. The electric field-tunable electronic and optical properties of the $P_2/MoSe_2$ vdW heterostructure make it a potential candidate for optoelectronic devices.

Conflicts of interest

There are no conflicts to declare.

Acknowledgements

This work is supported by the Research Fund (No. 1052931610) of Jiangsu University of Science and Technology.

References

1 C. V. Nguyen, M. Idrees, H. V. Phuc, N. N. Hieu, N. T. T. Binh, B. Amin and T. V. Vu, *Phys. Rev. B*, 2020, **101**, 235419.
2 T. V. Vu, N. V. Hieu, H. V. Phuc, N. N. Hieu, H. D. Bui, M. Idrees, B. Amin and C. V. Nguyen, *Appl. Surf. Sci.*, 2020, **507**, 145036.
3 I. Shahid, S. Ahmad, N. Shehzad, S. Yao, C. V. Nguyen, L. Zhang and Z. Zhou, *Appl. Surf. Sci.*, 2020, **523**, 146483.
4 S. Fan, Q. A. Vu, M. D. Tran, S. Adhikari and Y. H. Lee, *2D Mater.*, 2020, **7**, 022005.
5 Q. Lv and R. Lv, *Carbon*, 2019, **145**, 240–250.
6 K. S. Novoselov, A. Mishchenko, A. Carvalho and A. H. Castro Neto, *Science*, 2016, **353**, aac9439.
7 H. Lim, S. I. Yoon, G. Kim, A.-R. Jang and H. S. Shin, *Chem. Mater.*, 2014, **26**, 4891–4903.
8 A. K. Geim and I. V. Grigorieva, *Nature*, 2013, **499**, 419.
9 X. Hong, J. Kim, S.-F. Shi, Y. Zhang, C. Jin, Y. Sun, S. Tongay, J. Wu, Y. Zhang and F. Wang, *Nat. Nanotechnol.*, 2014, **9**, 682.
10 Q. Zheng, W. A. Saidi, Y. Xie, Z. Lan, O. V. Prezhdo, H. Petek and J. Zhao, *Nano Lett.*, 2017, **17**, 6435–6442.
11 X. Niu, Y. Li, Y. Zhang, Q. Zheng, J. Zhao and J. Wang, *J. Mater. Chem. C*, 2019, **7**, 1864–1870.
12 P. Rivera, J. R. Schaibley, A. M. Jones, J. S. Ross, S. Wu, G. Aivazian, P. Klement, K. Seyler, G. Clark, N. J. Ghimire, J. Yan, D. G. Mandrus, W. Yao and X. Xu, *Nat. Commun.*, 2015, **6**, 6242.
13 B. Miller, A. Steinhoff, B. Pano, J. Klein, F. Jahnke, A. Holleitner and U. Wurstbauer, *Nano Lett.*, 2017, **17**, 5229–5237.
14 L. Britnell, R. M. Ribeiro, A. Eckmann, R. Jalil, B. D. Belle, A. Mishchenko, Y.-J. Kim, R. V. Gorbachev, T. Georgiou, S. V. Morozov, A. N. Grigorenko, A. K. Geim, C. Casiraghi, A. H. C. Neto and K. S. Novoselov, *Science*, 2013, **340**, 1311–1314.
15 Y. Deng, Z. Luo, N. J. Conrad, H. Liu, Y. Gong, S. Najmaei, P. M. Ajayan, J. Lou, X. Xu and P. D. Ye, *ACS Nano*, 2014, **8**, 8292–8299.
16 P. Xiong, X. Zhang, H. Wan, S. Wang, Y. Zhao, J. Zhang, D. Zhou, W. Gao, R. Ma, T. Sasaki and G. Wang, *Nano Lett.*, 2019, **19**, 4518–4526.
17 Z. Yuan, J. Li, M. Yang, Z. Fang, J. Jian, D. Yu, X. Chen and L. Dai, *J. Am. Chem. Soc.*, 2019, **141**, 4972–4979.
18 Y.-T. Du, X. Kan, F. Yang, L.-Y. Gan and U. Schwingenschlögl, *ACS Appl. Mater. Interfaces*, 2018, **10**, 32867–32873.
19 C. Zhao, C. Yu, B. Qiu, S. Zhou, M. Zhang, H. Huang, B. Wang, J. Zhao, X. Sun and J. Qiu, *Adv. Mater.*, 2018, **30**, 1702486.
20 X. Wang, H. Li, H. Li, S. Lin, J. Bai, J. Dai, C. Liang, X. Zhu, Y. Sun and S. Dou, *J. Mater. Chem. A*, 2019, **7**, 2291–2300.
21 W. Liu, Z. Wang, Y. Su, Q. Li, Z. Zhao and F. Geng, *Adv. Energy Mater.*, 2017, **7**, 1602834.
22 L. Huang, N. Huo, Y. Li, H. Chen, J. Yang, Z. Wei, J. Li and S.-S. Li, *J. Phys. Chem. Lett.*, 2015, **6**, 2483–2488.
23 N. Lu, H. Guo, L. Li, J. Dai, L. Wang, W.-N. Mei, X. Wu and X. C. Zeng, *Nanoscale*, 2014, **6**, 2879.
24 L. Huang and J. Li, *Appl. Phys. Lett.*, 2016, **108**, 083101.
25 D. Chen, X. Lei, Y. Wang, S. Zhong, G. Liu, B. Xu and C. Ouyang, *Appl. Surf. Sci.*, 2019, **497**, 143809.
26 K. Rahimi, *Phys. Chem. Chem. Phys.*, 2020, **22**, 7412–7420.
27 S. Gao, L. Yang and C. D. Spataru, *Nano Lett.*, 2017, **17**, 7809–7813.
28 Y. Li, J.-K. Qin, C.-Y. Xu, J. Cao, Z.-Y. Sun, L.-P. Ma, P. A. Hu, W. Ren and L. Zhen, *Adv. Funct. Mater.*, 2016, **26**, 4319–4328.
29 S. Tongay, J. Zhou, C. Ataca, K. Lo, T. S. Matthews, J. Li, J. C. Grossman and J. Wu, *Nano Lett.*, 2012, **12**, 5576–5580.
30 J. S. Ross, S. Wu, H. Yu, N. J. Ghimire, A. M. Jones, G. Aivazian, J. Yan, D. G. Mandrus, D. Xiao, W. Yao and X. Xu, *Nat. Commun.*, 2013, **4**, 1474.
31 M. Bernardi, M. Palummo and J. C. Grossman, *Nano Lett.*, 2013, **13**, 3664–3670.
32 B. Chamlagain, Q. Li, N. J. Ghimire, H.-J. Chuang, M. M. Perera, H. Tu, Y. Xu, M. Pan, D. Xaio, J. Yan, D. Mandrus and Z. Zhou, *ACS Nano*, 2014, **8**, 5079–5088.

 This journal is © The Royal Society of Chemistry 2020

Open Access Article. Published on 25 July 2020. Downloaded on 12/30/2025 10:04:13 AM.
This article is licensed under a Creative Commons Attribution-NonCommercial 3.0 Unported Licence.

33 J. L. Zhang, S. Zhao, C. Han, Z. Wang, S. Zhong, S. Sun, R. Guo, X. Zhou, C. D. Gu, K. D. Yuan, Z. Li and W. Chen, *Nano Lett.*, 2016, **16**, 4903–4908.
34 J. Guan, Z. Zhu and D. Tománek, *Phys. Rev. Lett.*, 2014, **113**, 046804.
35 Z. Zhu and D. Tománek, *Phys. Rev. Lett.*, 2014, **112**, 176802.
36 B. Ghosh, S. Nahas, S. Bhowmick and A. Agarwal, *Phys. Rev. B: Condens. Matter Mater. Phys.*, 2015, **91**, 115433.
37 J. Xiao, M. Long, X. Zhang, J. Ouyang, H. Xu and Y. Gao, *Sci. Rep.*, 2015, **5**, 9961.
38 A. Ramasubramaniam, *Phys. Rev. B: Condens. Matter Mater. Phys.*, 2012, **86**, 115409.
39 D. Kozawa, A. Carvalho, I. Verzhbitskiy, F. Giustiniano, Y. Miyauchi, S. Mouri, A. H. Castro Neto, K. Matsuda and G. Eda, *Nano Lett.*, 2016, **16**, 4087–4093.
40 E. M. Alexeev, D. A. Ruiz-Tijerina, M. Danovich, M. J. Hamer, D. J. Terry, P. K. Nayak, S. Ahn, S. Pak, J. Lee, J. I. Sohn, M. R. Molas, M. Koperski, K. Watanabe, T. Taniguchi, K. S. Novoselov, R. V. Gorbachev, H. S. Shin, V. I. Fal'ko and A. I. Tartakovskii, *Nature*, 2019, **567**, 81–86.
41 P. K. Nayak, Y. Horbatenko, S. Ahn, G. Kim, J.-U. Lee, K. Y. Ma, A.-R. Jang, H. Lim, D. Kim, S. Ryu, H. Cheong, N. Park and H. S. Shin, *ACS Nano*, 2017, **11**, 4041–4050.
42 S. Goedecker, M. Teter and J. Hutter, *Phys. Rev. B: Condens. Matter Mater. Phys.*, 1996, **54**, 1703–1710.
43 P. Giannozzi, S. Baroni, N. Bonini, M. Calandra, R. Car, C. Cavazzoni, D. Ceresoli, G. L. Chiarotti, M. Cococcioni, I. Dabo, A. Dal Corso, S. de Gironcoli, S. Fabris, G. Fratesi, R. Gebauer, U. Gerstmann, C. Gougoussis, A. Kokalj, M. Lazzeri, L. Martin-Samos, N. Marzari, F. Mauri, R. Mazzarello, S. Paolini, A. Pasquarello, L. Paulatto, C. Sbraccia, S. Scandolo, G. Sclauzero, A. P. Seitsonen, A. Smogunov, P. Umari and R. M. Wentzcovitch, *J. Phys.: Condens. Matter*, 2009, **21**, 395502.
44 J. P. Perdew, K. Burke and M. Ernzerhof, *Phys. Rev. Lett.*, 1996, **77**, 3865–3868.
45 M. Dion, H. Rydberg, E. Schröder, D. C. Langreth and B. I. Lundqvist, *Phys. Rev. Lett.*, 2004, **92**, 246401.
46 M. Dion, H. Rydberg, E. Schröder, D. C. Langreth and B. I. Lundqvist, *Phys. Rev. Lett.*, 2005, **95**, 109902.
47 L. Bengtsson, *Phys. Rev. B: Condens. Matter Mater. Phys.*, 1999, **59**, 12301–12304.
48 S. Baroni, S. de Gironcoli, A. Dal Corso and P. Giannozzi, *Rev. Mod. Phys.*, 2001, **73**, 515–562.
49 L. Hedin, *Phys. Rev.*, 1965, **139**, A796–A823.
50 E. E. Salpeter and H. A. Bethe, *Phys. Rev.*, 1951, **84**, 1232.
51 M. Rohlfing and S. G. Louie, *Phys. Rev. B: Condens. Matter Mater. Phys.*, 2000, **62**, 4927–4944.
52 A. Marini, C. Hogan, M. Grüning and D. Varsano, *Comput. Phys. Commun.*, 2009, **180**, 1392–1403.
53 T. Böker, R. Severin, A. Müller, C. Janowitz, R. Manzke, D. Voß, P. Krüger, A. Mazur and J. Pollmann, *Phys. Rev. B: Condens. Matter Mater. Phys.*, 2001, **64**, 235305.
54 M. M. Ugeda, A. J. Bradley, S.-F. Shi, F. H. da Jornada, Y. Zhang, D. Y. Qiu, W. Ruan, S.-K. Mo, Z. Hussain, Z.-X. Shen, F. Wang, S. G. Louie and M. F. Crommie, *Nat. Mater.*, 2014, **13**, 1091–1095.
55 A. J. Bradley, M. M. Ugeda, F. H. da Jornada, D. Y. Qiu, W. Ruan, Y. Zhang, S. Wickenburg, A. Riss, J. Lu, S.-K. Mo, Z. Hussain, Z.-X. Shen, S. G. Louie and M. F. Crommie, *Nano Lett.*, 2015, **15**, 2594–2599.
56 C. E. P. Villegas, A. S. Rodin, A. Carvalho and A. R. Rocha, *Phys. Chem. Chem. Phys.*, 2016, **18**, 27829–27836.
57 The AM 1.5G Spectrum Was Taken from the NREL Website: http://Rredc.Nrel.Gov/Solar/Spectra/Am1.5 and Integrated with the Trapezoid Rule.
58 Y. Gong, J. Lin, X. Wang, G. Shi, S. Lei, Z. Lin, X. Zou, G. Ye, R. Vajtai, B. I. Yakobson, H. Terrones, M. Terrones, B. K. Tay, J. Lou, S. T. Pantelides, Z. Liu, W. Zhou and P. M. Ajayan, *Nat. Mater.*, 2014, **13**, 1135–1142.
59 B.-J. Wang, X.-H. Li, R. Zhao, X.-L. Cai, W.-Y. Yu, W.-B. Li, Z.-S. Liu, L.-W. Zhang and S.-H. Ke, *J. Mater. Chem. A*, 2018, **6**, 8923–8929.
60 B.-J. Wang, X.-H. Li, X.-L. Cai, W.-Y. Yu, L.-W. Zhang, R.-Q. Zhao and S.-H. Ke, *J. Phys. Chem. C*, 2018, **122**, 7075–7080.
61 N. A. Lanzillo, A. J. Simbeck and S. K. Nayak, *J. Phys.: Condens. Matter*, 2015, **27**, 175501.
62 F. Ceballos, M. Z. Bellus, H.-Y. Chiu and H. Zhao, *ACS Nano*, 2014, **8**, 12717–12724.
63 S. Tongay, W. Fan, J. Kang, J. Park, U. Koldemir, J. Suh, D. S. Narang, K. Liu, J. Ji, J. Li, R. Sinclair and J. Wu, *Nano Lett.*, 2014, **14**, 3185–3190.
64 M.-H. Chiu, M.-Y. Li, W. Zhang, W.-T. Hsu, W.-H. Chang, M. Terrones, H. Terrones and L.-J. Li, *ACS Nano*, 2014, **8**, 9649–9656.